# Observation of the dynamic modes of a magnetic antivortex using Brillouin light scattering

Grant A. Riley, H. J. Jason Liu, Martin A. Asmat-Uceda, Arabinda Haldar, and Kristen S. Buchanan

Phys. Rev. B **92**, 064423 — Published 26 August 2015

DOI: 10.1103/PhysRevB.92.064423

# Observation of the dynamic modes of a magnetic antivortex using Brillouin light scattering

Grant A. Riley,[1] H.J. Jason Liu,[1] Martin A. Asmat-Uceda,[1] Arabinda Haldar,[1] and Kristen S. Buchanan[1,*]

[1]*Department of Physics, Colorado State University, Fort Collins, Colorado 80523, USA*

The dynamic behavior of magnetic antivortices stabilized in patterned pound-key-like microstructures was studied using micro-focus Brillouin light scattering (micro-BLS) at frequencies above the gyrotropic mode (>1 GHz). Micro-BLS spectra obtained as a function of the frequency of a driving microwave field show an intricate spectrum for the antivortex state for an in-plane driving field. Spatial mode profiles for the strongest antivortex resonance frequencies, obtained for samples in the antivortex as well as the single domain states, show that while the symmetry of one of the observed resonances is relatively insensitive to the spin configuration, the antivortex exhibits a unique mode profile for the other. A comparison with micromagnetic simulations shows that the frequency and symmetry of the latter are consistent with one of the antivortex azimuthal modes. Furthermore, the simulations show that this mode involves coupling between the antivortex spin excitations and propagating spin waves in the structure legs, which may be useful for high-wavenumber spin wave generation.

*PACS: 75.75.-c, 74.25.Ha, 76.50.+g*

* Author to whom correspondence should be addressed: Kristen.Buchanan@colostate.edu

## I. Introduction

Exotic spin textures in patterned magnetic nanostructures are currently attracting a great deal of attention because they exhibit a variety of interesting physical properties and show promise for applications. By controlling the material properties, geometry, and the external field history, it is possible to form and stabilize topologically non-uniform magnetic states such as magnetic vortices [1,2], antivortices [3-5], and more exotic states such as skyrmions [6]. The magnetic vortex and its topological counterpart, the magnetic antivortex (AV), both possess an out-of-plane core region, which has two distinct binary states – up or down. Due to its flux-closure magnetic configuration the vortex state is often a low energy or ground state in magnetically soft magnetic structures, whereas the AV state (Fig. 1), which involves spins that sweep in from two opposite sides (e.g. the top and bottom) and out from the other two (e.g., left and right), is metastable and more difficult to create as an isolated entity [3-5,7]. The AV state has received considerably less attention than the vortex state, even though simulations suggest that AV's should have similarly rich dynamics [8] and may, in fact, have higher potential for driving spin-waves [7,9,10]. Vortices exhibit a variety of interesting dynamic properties that include sub-gigahertz gyrotropic motion driven by magnetic fields [11-13] or spin polarized currents [14-16], higher frequency (>1 GHz) quantized spin excitations [17,18], long range magnetostatic coupling interactions [19,20], dynamic core reversal [21,22], and selective ordering effects [23]. Simulated results and analytical models have shown that the AV core will gyrate and that the polarity will reverse when driven by a suitable in-plane magnetic field or a spin-polarized current [9,24-27]. While these low-frequency processes have been observed experimentally [25,28,29], the only studies that have been done thus far on the high-frequency spin dynamics of the AV are theoretical [8].

In this work, micro-focus Brillouin light scattering (micro-BLS) spectroscopy, which can be used to obtain frequency-resolved information on dynamics in magnetic materials via inelastic light scattering with diffraction-limited spatial resolution [30], was used to investigate the dynamics of magnetic AV's in Permalloy microstructures. Measurements conducted as a function of frequency reveal a rich spectrum for the AV's and spatial imaging combined with micromagnetic simulations provide additional insight into the observed modes.

## II. Experiment

To investigate the dynamics of the magnetic AV state, pound-key-like magnetic microstructures made of Permalloy ($Ni_{80}Fe_{20}$) were fabricated on top of an 18-μm wide, 250-nm thick gold strip-line waveguide using electron beam lithography,

magnetron sputtering, and liftoff. Figure 1 shows the experimental setup as well as magnetic force microscopy (MFM) images of the structures that were investigated. The sample dimensions, as defined in Fig. 1, are: $L$ = 6 μm, $b$ = 2 μm, $w$ = 1 μm, and the thickness is 37 nm. Atomic force microscopy measurements show that the surface roughnesses of the gold waveguide and the patterned Permalloy structures are 3.5 and 5.0 nm, respectively. The differences in the shape anisotropy in the wide and narrow sections of structures with this general shape can be used to influence the reversal process and hence to promote the nucleation of magnetic AV's, as described in Refs. [5,31]. The AV's were prepared by applying first a saturating field and then a smaller field in the opposite direction along the structure diagonal that runs through the wider legs. As shown in the MFM images, two AV's were present in the samples ($AV_1$ and $AV_2$), identified based on the hourglass-like contrast observed at these two intersections. For details on the factors that influence the AV formation success rate including the role of the sample geometry and the angle of the applied field, refer to Ref. [31]. In Fig. 1 the other intersections are saturated parallel ($Sat_{\parallel}$) and perpendicular ($Sat_{\perp}$) to the in-plane driving magnetic field $h$. MFM imaging was performed before and after the micro-BLS measurements to confirm that the spin configuration of the samples remained the same.

The sample was excited using a microwave field $h$, applied along the structure diagonal as illustrated in Fig. 1. A microwave power of 13 dBm, which corresponds to $h \approx 0.6$ mT, was used for all measurements. At this power the structures exhibit a linear response within the frequency range that was considered (1 to 7 GHz). Micro-BLS measurements were made as a function of the microwave pumping frequency $f_P$ for each of the intersections shown in Fig. 1 at a fixed point that was slightly offset from the center of the intersection (see inset of Fig. 2). An off-center point was chosen because the resonances of interest involve motion within the intersection but the amplitude tends to be larger away from the core. The spatial resolution of the micro-BLS is ~300 nm and spin excitations with wavevectors of up to 20 $\mu m^{-1}$ (minimum wavelength $\lambda \sim 0.3$ μm) [32] can be detected. Two-dimensional spatial measurements were made for intersections in the AV as well as the saturated states at selected frequencies using a 2D grid of 10 x 10 points centered on the intersections.

## III. Results

### A. Experimental Measurements

Figure 2 shows micro-BLS measurements for each of the AV, $Sat_{\parallel}$, and $Sat_{\perp}$ states as a function of $f_P$, measured over a frequency range from 1 to 7 GHz in 100 MHz increments. The BLS intensities shown here were obtained by integrating each spectrum over the range $f_P \pm 350$ MHz and then normalizing to a reference signal that is proportional to the

power of the incident laser beam to account for any fluctuations in the laser intensity. As shown in Fig. 2, the intensity of the strongest $Sat_{\perp}$ resonance is >10,000 counts as compared to ~1,700 for the AV and $Sat_{\parallel}$ states. The higher intensity for the $Sat_{\perp}$ state occurs because the spins in the intersection are mainly perpendicular to *h* and consequently the torque is large. The most notable feature of the AV signal in Fig. 2 is the peak near 5.9 GHz. This is the strongest feature for all of the magnetic states in this frequency range and it is relatively wide with several sharper peaks, which suggests that there are multiple closely spaced modes within this range. In addition to the strong peak at 5.9 GHz, the AV state also exhibits a resonance at 3.4 GHz that is well above the noise level. Other features in the AV spectrum include weak activity just below 3 GHz, most notably at 2.8 GHz, a broad response from 3.9-4.5 GHz that shows peaks at 4.0 and 4.3 GHz, and peaks at 5.2 and 6.2 GHz that blend in with the stronger resonance at 5.9 GHz. The saturated configurations also exhibit activity within multiple frequency ranges. The $Sat_{\perp}$ state shows activity in the range of 1.5-2.5 GHz with a peak at 2.3 GHz, from 3.9-5.3 GHz with peaks at 4.6 and 5.1 GHz, and broad activity above 5.3 GHz that tapers above 6 GHz and shows a strong peak at 5.7 GHz that is close in frequency to the 5.9 GHz peak observed for the AV state. The $Sat_{\parallel}$ state shows an almost identical response to $Sat_{\perp}$ above 5.3 GHz but comparatively little activity at lower frequencies with weak peaks at 4.1 and 4.7 GHz and considerably reduced signal below 2.8 GHz, suggesting that much of the $Sat_{\perp}$ signal observed in the low frequency range is related to the intersection rather than the leg regions. Here the measurements conducted on the saturated state are mainly used to compare with response of the AV state; a detailed examination of the resonances of the saturated states is beyond the scope of this paper.

To further characterize the modes, spatial scans at selected $f_P$ were conducted. Figure 3 shows the normalized BLS intensity as a function of position for a 1.2x1.2 $\mu m^2$ square that is slightly larger than the intersection region, as illustrated in Fig. 3a, 3d, and 3g, for two of the prominent modes observed in Fig. 2, one at 3.4 GHz and the other at 5.9 GHz. The former was chosen since the frequency scans indicate that at 3.4 GHz the AV shows a strong resonance while the other states exhibit proportionally less activity, and 5.9 GHz was chosen since the most prominent mode for all three states occurs at or close to this frequency. The spatial profiles obtained at 3.4 GHz are different for all three states. For the AV (Fig. 3b) the largest signals are observed near the center of each of the four sides of the intersection region. The mode shows quasi-four-fold symmetry in that the shapes of the intensity profiles on each of the four sides are similar. The peak intensities in the different quadrants do, however, differ significantly. This may be due to the fact that the inner and outer legs have different lengths, which could lead to an asymmetry in the resonance. The $Sat_{\parallel}$ state (Fig. 3e) shows little signal, whereas a large, slightly off-

center signal is observed within the intersection region for $\mathrm{Sat}_\perp$ (Fig. 3h) that corresponds to the region where the spins are mainly perpendicular to *h*. Both $\mathrm{Sat}_\parallel$ and $\mathrm{Sat}_\perp$ show some intensity within each of the legs but the signal is farther from the intersection as compared to that observed for the AV. At 5.9 GHz, the mode profiles observed for the AV, $\mathrm{Sat}_\parallel$, and $\mathrm{Sat}_\perp$ states (shown in Fig. 3c, 3f, and 3i, respectively) are similar in that they exhibit a strong response near the legs and a lesser response within the intersection that is strongest for the $\mathrm{Sat}_\perp$ state.

### B. Numerical Simulations

Micromagnetic simulations were performed for a structure with the same geometry and dimensions as used in the experiments (12x12 $\mu m^2$ and 37-nm thick) using MuMax3 [33] to gain additional insight into the observed modes. A discretization mesh of 4x4x37 $nm^3$ was used with magnetic parameters typical for Permalloy: saturation magnetization $M_s$ = $8.0 \times 10^5$ A/m, exchange stiffness constant A = $1.3 \times 10^{-11}$ J/m, gyromagnetic ratio $\gamma = 1.76 \times 10^{11}$ $s^{-1}T^{-1}$ and zero magneto-crystalline anisotropy. Simulations conducted on smaller structures with additional discretization across the sample thickness indicate that a 2D mesh is sufficient to capture the dynamics of interest. An initial state with an AV at one intersection and a saturated configuration at the other was used, which yields a simulated MFM contrast that is in good agreement with Fig. 1. The $\mathrm{Sat}_\parallel$ state rather than the $\mathrm{Sat}_\perp$ was chosen for the dynamic simulations because it lacks the strong central intensity mode that is observed for latter, hence it provides a more useful comparison to the AV state. The spin configuration was first relaxed to equilibrium with no magnetic field using a damping constant $\alpha = 1$, and then the dynamic response to a Gaussian magnetic field pulse 30 ps in duration (full width at half of the maximum) and 0.1 mT in amplitude was simulated using a realistic damping constant of $\alpha = 0.01$. The pulse was applied in-plane along the structure diagonal and the short duration was chosen to suppress the gyrotropic mode in order to focus on the higher frequency dynamics (>1 GHz). The simulations were repeated at selected frequencies using an in-plane sinusoidal driving field (as in the experiment), which yielded steady state behavior that is essentially the same as the mode maps obtained by cell-by-cell Fourier analysis of the pulsed simulations.

Figure 4a shows simulated frequency spectra for the AV and $\mathrm{Sat}_\parallel$ states obtained in response to the in-plane pulsed magnetic field. These spectra represent the amplitude of the Fourier transform of the out-of-plane component of the magnetization $M_z$ that are averaged over 200x200 $nm^2$ subregions that were chosen to approximate the position of the laser spot that was used in the experiment (see the blue and green spots in the inset diagrams). For the AV, notable resonances

appear at frequencies of 1.90, 2.22, 3.08, 3.27, and 3.74 GHz. There is also broad activity with multiple peaks over the range from 4.3-4.9 GHz, a strong, broad, peak at 5.44 GHz and a lower amplitude peak at 6.30 GHz. The gyrotropic mode is also weakly excited in the simulations at a frequency of 120 MHz (not shown). Similar to what is observed in the experiments, the $\mathrm{Sat}_{\parallel}$ state shows a strong peak at close to but slightly below the frequency of the strongest AV peak (5.44 GHz), a general trend of reduced response with decreasing frequency is observed, and there is essentially no activity below 2.5 GHz.

Calculated mode maps are shown in Fig. 4b-4m for several of the prominent AV resonance frequencies where the Fourier amplitudes are shown for the AV and the $\mathrm{Sat}_{\parallel}$ states in the left and right columns, respectively. Note that these are mainly off-resonance mode profiles for the saturated states since the frequencies were chosen based on the AV spectrum. Animations of the most prominent modes are included as Supplementary Information [34]. Two different types of modes are observed for the AV state: those that involve resonances of just the AV region (1.90 and 2.22 GHz), and those that involve activity within both the AV and the legs that extend outward from the central region (>3 GHz). Several modes have both standing and propagating character and in some cases, for example, for the mode at 3.27 GHz, it appears that the AV region may act as the center of radiation for excitations that propagate outward along the legs.

The AV modes observed at 1.90 and 2.22. GHz both have cross-shaped amplitude patterns (Fig. 4b and 4d). The wavelength along the diagonal is approximately twice the distance from the corners of the intersection region to the central AV core. These modes circulate around the AV core in the counterclockwise and clockwise directions, respectively, for positive core polarity and they are similar to the lowest order ($n = 1$ where $n$ is the mode number) azimuthal modes that are described in Ref. [8] for an astroid-shaped ferromagnet. The $\mathrm{Sat}_{\parallel}$ state, in contrast, exhibits weak (low amplitude) standing spin wave motion at both of these frequencies (Fig. 4c and 4e) that occurs mainly in the regions where the spins tilt as they enter or exit the intersection. The AV modes at 3.08 GHz (see animation in Supplementary Information) and 3.27 GHz (Fig. 4f) are similar to the 1.90 and 2.22 GHz modes in that the highest amplitude response is along the intersection diagonals, except in this case the wavelength along the intersection diagonals is half of what it is for the $n = 1$ case. The modes appear to circulate counterclockwise for the lower frequency of the mode pair and clockwise for the higher, although is perhaps more easily viewed as spin waves that propagate along the diagonal. Either way, the modes have a handedness and these are the $n = 2$ azimuthal modes. Unlike the $n = 1$ modes, however, the dynamics are no longer confined to just the intersection region - motion is also visible in the legs of the structure. Spin waves are visible in the legs for the 3.08 GHz and 3.27 GHz modes, which are stronger for the latter mode. The spin waves along the legs are quantized across the leg width with a single,

central antinode ($m = 1$ mode, where $m$ is the integer mode number across the leg width), which is expected for confined microstrips [35]. The wavelength along the legs is approximately 0.32 µm, slightly smaller than $w/2$, which is the approximate leg-directed component of the wavelength of the $n = 2$ excitation within the AV region. Activity is also evident in the leg regions for the $\mathrm{Sat}_{\parallel}$ except the wavelength is longer, the peak amplitude is farther from the intersection, and the animations show that the direction of propagation is towards the intersection, opposite to that observed for the AV state. This can be understood by considering the properties of the dispersion curves for long microstrips magnetized along their length, the backward volume spin wave geometry, which will be discussed in more detail below.

For the higher frequency AV modes (3.74, 4.32, and 5.44 GHz) the simulations show increasing activity in the legs, a trend that is also observed in the simulations of the $\mathrm{Sat}_{\parallel}$ state at the same frequencies. The wavevector components along the structure legs tend to increase with increasing frequency and the mode number within the legs also increases with frequency, where $m = 1$ leg modes are observed from 3.1 to 4.3 GHz and at 5.44 GHz the $m = 2$ leg mode dominates. Distinct modes are more difficult to identify in both the frequency spectra and the spatially-resolved mode maps for this frequency range ($\geq$ 3.74 GHz). The peaks at 3.74 and 4.32 GHz (Fig 4h and 4j) show motion along the diagonals that is similar to what is observed for the azimuthal modes but the wavelength is shorter and there is also increased activity between the intersection diagonals. For these modes as well as the 5.44 GHz mode (Fig. 4l), the highest amplitude motion within the intersection occurs near the two corners at the top left and bottom right where the motion in these regions is 180 degrees out-of-phase across the diagonal (see animations), which is related to the symmetry of the spin distribution and the direction of the excitation field.

## IV. Discussion

The modes observed experimentally at 3.4 and 5.9 GHz (Fig. 3) are closest in frequency to the simulated modes found at 3.27 and 5.44 GHz (Fig. 4f and 4l), respectively. Since the BLS is sensitive to wavevectors associated with features with spatial wavelengths of ~0.3 µm or larger, the finer details near the AV core and near the corners are not expected to be resolved by the experiments, hence the main symmetries of the experimental AV modes shown in Fig. 3b and 3c are in reasonable agreement with the simulated modes shown in Fig. 4f and 4l, respectively. In general, a number of closely spaced modes with complex spin distributions are observed in the higher frequency range so it is more difficult to identify the exact mode associated with the 5.9 GHz experimental resonance, however, the peak in the simulations at 5.44 GHz and in the

experiment at 5. 9 GHz are similarly strong features in the frequency spectra (Fig 4a and Fig. 2, respectively). Furthermore, at 5.44 GHz, the AV and $Sat_{\parallel}$ states (Fig. 4l and 4m) both show similar behavior in the leg regions and both states also have mainly short-wavelength activity in the intersection that may lead to a lower BLS signal in this region. In the simulated $Sat_{\parallel}$ response at 3.27 GHz (Fig. 4g) the area of main activity is shifted further down the legs as compared to the AV response (Fig. 4f) in agreement with experimental observations at 3.4 GHz and there is an asymmetry in the intensity distribution of the simulated AV mode that is similar to what is observed experimentally. Additional simulations show that the corresponding AV mode takes on a symmetric shape in a symmetric cross structure suggesting that the observed mode asymmetry is caused by the structure shape.

The simulated AV frequency spectrum shows additional features at lower frequencies and while some are similar to the experimental measurements shown in Fig. 2, there are also differences. The broad peaks observed in the experiments at 4.0 and 4.3 GHz are similar in frequency and form to the simulated peaks at 3.74 and 4.32 GHz, respectively. There are several additional peaks in the simulated frequency spectrum at the other azimuthal mode frequencies (1.90, 2.22, and 3.08 GHz) that are more prominent in the simulations than in the experiments. There is a weak peak in the experimental AV spectrum at 2.8 GHz that may correspond to the lower frequency $n = 2$ azimuthal mode (3.08 GHz in the simulations). There are no particularly prominent features in experimental AV spectrum below 2.8 GHz, however, additional frequency scans conducted at several other points within the intersection show stronger activity at 2.9 GHz as well as two additional peaks at 1.7 and 2.3 GHz (not shown), suggesting that the reason that the lower frequency azimuthal modes are difficult to identify in Fig. 2 is likely related to the details of how the spectra vary spatially within the structure.

For magnetic vortices, two main types of dynamic modes are observed at frequencies above the gyrotropic resonance (>1 GHz): modes with radial [17,18] and azimuthal [36] symmetries, whereas for in-plane magnetized wires, the spin excitations are often discussed in terms of backward volume (BV) vs. Damon Eschbach (DE) modes where the magnetization is along the wire (and the spin wave wavevector) for the former and perpendicular for the latter. Simulations of the AV dynamics in astroid structures have been classified in a similar manner where the "radial" modes are standing spin wave excitations and the "azimuthal" modes have some propagating character as well [8]. Unlike the astroid geometry considered in Ref. [8], an AV in a pound-key-like structure is connected to extended micro-wires. In the pound-key-like structures the magnetization direction extends smoothly from the AV core and into the legs so is possible to have BV-type excitations that will propagate along the legs. In the legs, the wavevectors of the spin waves observed in the simulations are

quantized across the leg width, which is expected for magnetic microstrips [35,37], where one ($m = 1$) and two ($m = 2$) antinodes are observed in Fig. 4f – 4k and Fig. 4l – 4m, respectively. BV dispersion curves calculated using Eq. [24] in Ref. [37] yield wavelengths along the wire of $\lambda = 0.32$ µm ($k = 20$ µm$^{-1}$) and $\lambda = 0.15$ µm ($k = 42$ µm$^{-1}$) for one antinode at f=3.27 GHz and two antinodes at f=5.44 GHz, respectively, both of which are close to the values observed in the simulations of $\lambda = 0.35$ and 0.15 µm, respectively [38]. Note that the minimum frequency allowed by the disperion curves occurs at 3.1 GHz, which explains why no significant activity is observed in the legs for either state at 1.90 or 2.22 GHz.

At 3.27 GHz the $\text{Sat}_{\parallel}$ state shows a longer wavelength (compared to the AV state) along the legs of $\lambda \sim 1$ µm and, as mentioned previously, the propagation direction is inward, opposite to that observed for the AV state. The wavelengths listed above are obtained from the higher-wavevector portion of the dispersion curve where exchange dominates and the spin wave group velocities are positive, however, backward volume spin wave dispersion curves first decrease and then increase with wavevector. Consequently there is another possible wavevector in the lower-k region, which is $\lambda = 0.62$ µm ($k = 10$ µm$^{-1}$) at 3.27 GHz and this corresponds to spin waves with a negative group velocity. Hence the larger wavelength and the difference in propagation direction observed for the $\text{Sat}_{\parallel}$ state are also consistent with expectations based on calculated dispersion curves. It is interesting that the different spin configurations within the intersection lead to quite different dominant leg modes for the same excitation frequency. Microstrip antennas have limited efficiency for exciting $\lambda < d/2$, where $d$ is the antenna width [39], which places practical limitations on the smallest wavelengths that can be easily excited. Not only do AV's exhibit dynamics that are quite different than the reported modes of a magnetic vortex, but the coupling between the AV modes and leg modes may also offer an alternative means to excite small-$\lambda$ spin waves.

## V. Conclusions

In summary, micro-BLS measurements of the dynamics of a magnetic AV stabilized in a patterned microstructure show a rich excitation spectrum. Micromagnetic simulations show that AV's will exhibit modes that have both standing and propagating characteristics and that the seamless transition from the AV spin configuration into the saturated legs of the structures used for this study leads to modes that originate in the AV region and propagate along the legs. One of the leg-coupled azimuthal modes found in the simulations occurs at a similar frequency and possesses a similar amplitude profile as compared to a strong resonance observed experimentally for the AV state. Both the simulations and experiments show that

the AV dynamics are more complex than that of a vortex but the unique topology of the AV state shows intriguing potential for the generation of propagating spin waves that may be of interest for magnonics applications.

**Acknowledgements**

We thank M. Wu for use of the magnetic force microscope. This research was supported by the U.S. Department of Energy, Office of Basic Energy Sciences, Division of Materials Sciences and Engineering under Award #ER 46854 (experiments and simulations) and the National Institute of Standards and Technology Grant #60NANB10D011 (development of the micro-BLS). Use of the Center for Nanoscale Materials was supported by the U. S. Department of Energy, Office of Science, Office of Basic Energy Sciences, under Contract No. DE-AC02-06CH11357.

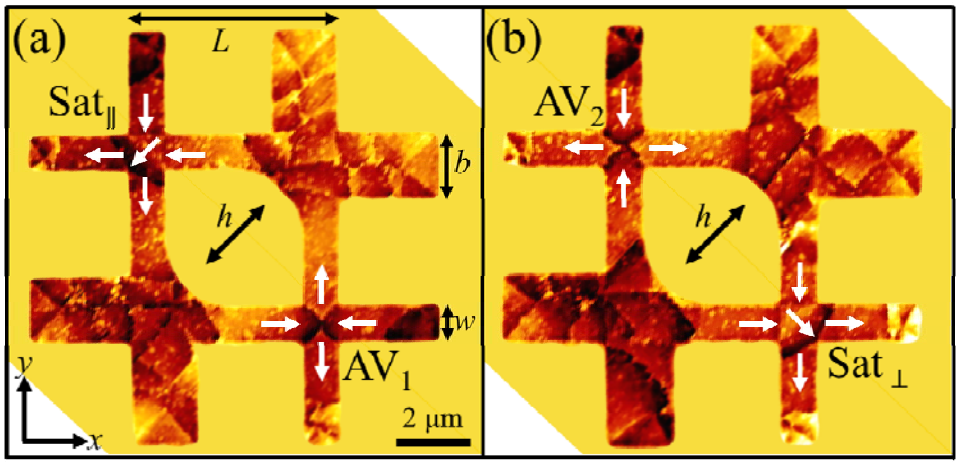


FIG 1. MFM images of two 37-nm thick Permalloy structures superimposed on a diagram of a waveguide to illustrate the experimental geometry. The upper left intersection in structure (a) is saturated parallel to the dynamic field $h$ ($Sat_{//}$) while the hourglass-like MFM contrast in the lower right intersection indicates that this intersection contains a single AV ($AV_1$). Structure (b) has an AV in the upper left intersection ($AV_2$) and is saturated perpendicular to $h$ in the lower right intersection ($Sat_{\perp}$). The white arrows indicate the direction of the magnetization.

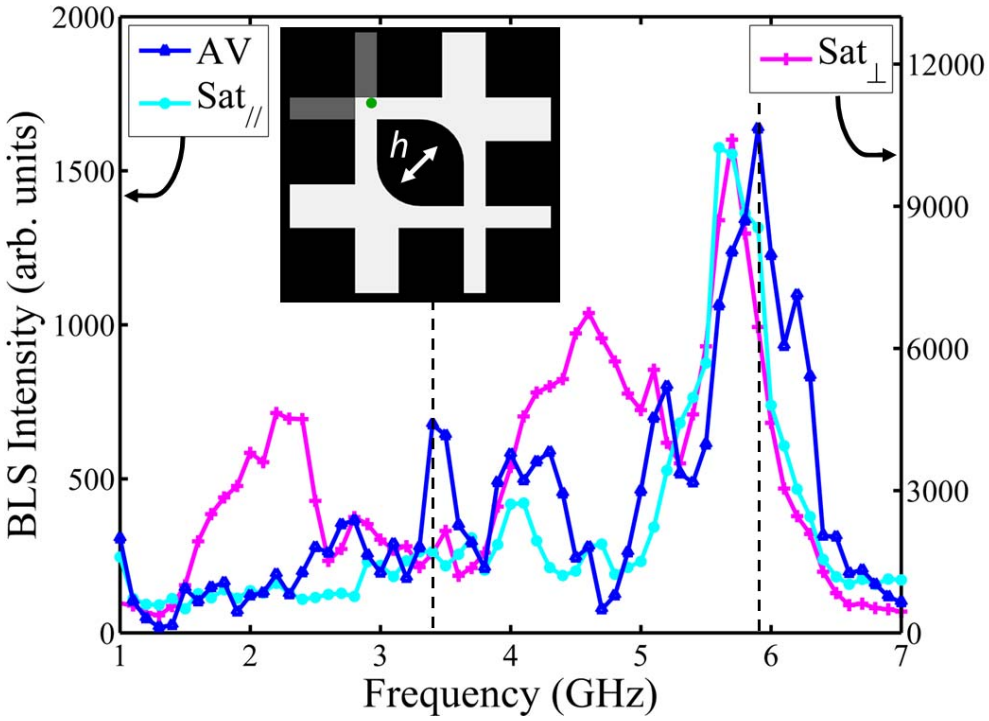


FIG 2. BLS intensity as a function of $f_P$ measured within the intersection regions of the pound-key-like structures. Data are shown for intersections in the AV, Sat$_{//}$, and Sat$_{\perp}$ states. The inset illustrates the position of the laser spot (shaded green spot), which is displaced from the center of the intersection towards one of the outer legs. The dashed lines at 3.4 GHz and 5.9 GHz show the frequencies at which spatial imaging was performed (Fig. 3).

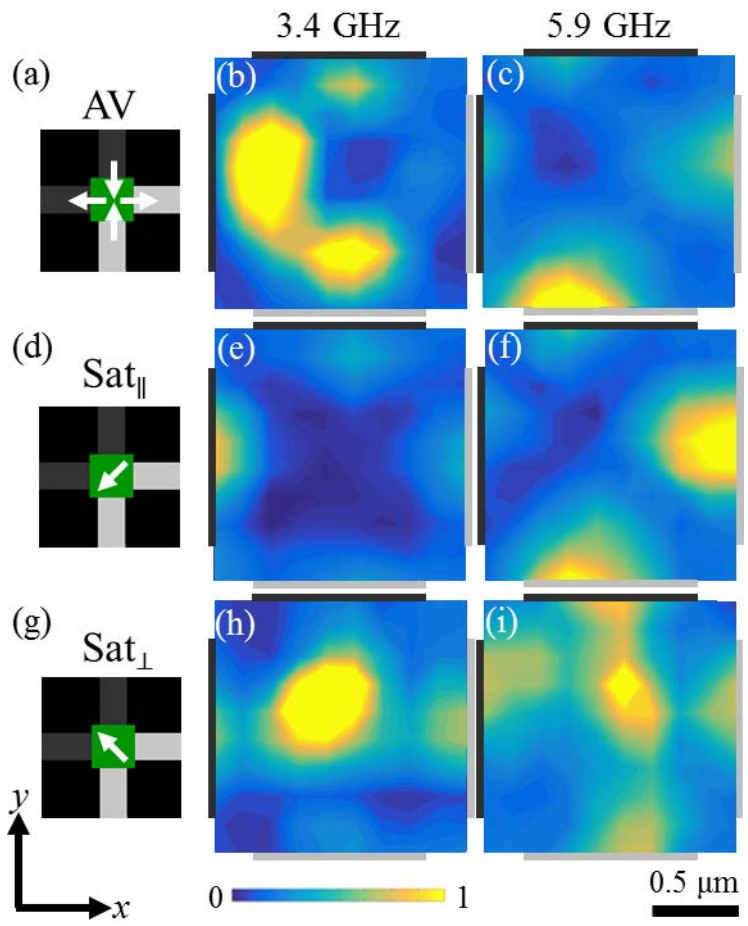


FIG 3. BLS Intensity as a function of position for a 2D grid of 10 x 10 points obtained over intersections in the AV (b, c), $Sat_{//}$ (e, f), and $Sat_{\perp}$ (h, i) states, where *h* is applied in-plane, along the diagonal, as illustrated in Fig. 2. The diagrams (a, d, and g) show the scan region (shaded in green), which is slightly larger than the intersection, and the white arrows illustrate the direction of the magnetization for each state. The dark and light gray shading on the diagrams and beside each of the BLS plots is used to identify the outer and inner legs of the structure, respectively, with respect to the scan region. BLS scans are shown for each state for $f_P$ = 3.4 GHz in the middle column (b, e, and h) and $f_P$ = 5.9 GHz in the right column (c, f, and i).

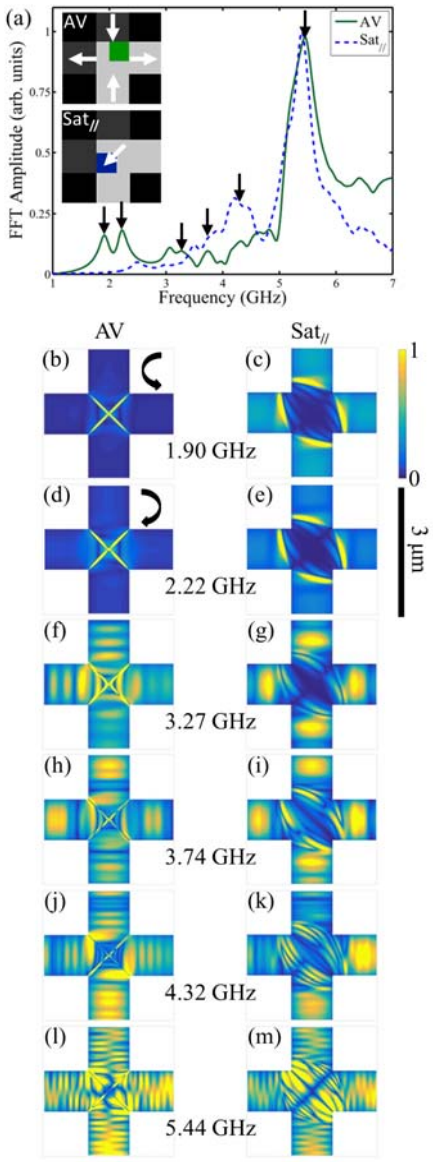


FIG 4. Frequency spectra (a) and spatially resolved modes (b-m) obtained from micromagnetic simulations for intersections that are in the AV (left) and Sat// (right) states in response to an in-plane magnetic field pulse applied along the structure diagonal. The frequency spectra shown in (a) represent the amplitude of the Fourier transform of the time dependent out-of-plane component of the magnetization $M_z$ in each cell, averaged over a 200x200 nm$^2$ sub-region within the intersection (locations marked by squares in the inset). In the inset, the dark and light shading indicates outer vs. inner legs of the structure, respectively, and the white arrows illustrate the spin configurations. The mode maps (b-m) show the normalized spectral amplitude of $M_z$ for a 3x3 μm$^2$ region centered on the intersection.

**References**


[1] R. P. Cowburn, D. K. Koltsov, A. O. Adeyeye, M. E. Welland, and D. M. Tricker, Phys. Rev. Lett. **83**, 1042 (1999).

[2] T. Shinjo, T. Okuno, R. Hassdorf, K. Shigeto, and T. Ono, Science **289**, 930 (2000).

[3] V. L. Mironov *et al.*, Phys. Rev. B **81**, 094436 (2010).

[4] M. Pues, M. Martens, T. Kamionka, and G. Meier, Appl. Phys. Lett. **100**, 162404 (2012).

[5] A. Haldar and K. S. Buchanan, Appl. Phys. Lett. **102**, 112401 (2013).

[6] A. Fert, V. Cros, and J. Sampaio, Nat Nano **8**, 152 (2013).

[7] A. Kunz, E. C. Breitbach, and A. J. Smith, J. of Appl. Phys. **105**, 07D502 (2009).

[8] H. Wang and C. E. Campbell, Phys. Rev. B **76**, 220407 (2007).

[9] A. Drews, B. Kruger, G. Meier, S. Bohlens, L. Bocklage, T. Matsuyama, and M. Bolte, Appl. Phys. Lett. **94**, 062504 (2009).

[10] S. Gliga, M. Yan, R. Hertel, and C. M. Schneider, Phys. Rev. B **77**, 060404 (2008).

[11] J. P. Park, P. Eames, D. M. Engebretson, J. Berezovsky, and P. A. Crowell, Phys. Rev. B **67**, 020403 (2003).

[12] S.-B. Choe, Y. Acremann, A. Scholl, A. Bauer, A. Doran, J. Stöhr, and H. A. Padmore, Science **304**, 420 (2004).

[13] V. Novosad, F. Y. Fradin, P. E. Roy, K. S. Buchanan, K. Y. Guslienko, and S. D. Bader, Phys. Rev. B **72**, 024455 (2005).

[14] K. Yamada, S. Kasai, Y. Nakatani, K. Kobayashi, H. Kohno, A. Thiaville, and T. Ono, Nat Mater **6**, 270 (2007).

[15] S. D. Pollard, L. Huang, K. S. Buchanan, D. A. Arena, and Y. Zhu, Nat. Commun. **3**, 1028, 1028 (2012).

[16] V. S. Pribiag, I. N. Krivorotov, G. D. Fuchs, P. M. Braganca, O. Ozatay, J. C. Sankey, D. C. Ralph, and R. A. Buhrman, Nat. Phys. **3**, 498 (2007).

[17] K. Perzlmaier, M. Buess, C. H. Back, V. E. Demidov, B. Hillebrands, and S. O. Demokritov, Phys. Rev. Lett. **94**, 057202 (2005).

[18] K. Vogt *et al.*, Phys. Rev. B **84**, 174401 (2011).

[19] K. S. Buchanan, P. E. Roy, M. Grimsditch, F. Y. Fradin, K. Y. Guslienko, S. D. Bader, and V. Novosad, Nat. Phys. **1**, 172 (2005).

[20] S. Sugimoto, Y. Fukuma, S. Kasai, T. Kimura, A. Barman, and Y. C. Otani, Phys. Rev. Lett. **106**, 197203 (2011).

[21] B. Van Waeyenberge *et al.*, Nature **444**, 461 (2006).

[22] M. Sproll *et al.*, Appl. Phys. Lett. **104**, 012409 (2014).

[23] S. Jain, V. Novosad, F. Y. Fradin, J. E. Pearson, V. Tiberkevich, A. N. Slavin, and S. D. Bader, Nat. Commun. **3**, 1330 (2012).

[24] S. Gliga, R. Hertel, and C. M. Schneider, J. of Appl. Phys. **103**, 07b115 (2008).

[25] T. Kamionka, M. Martens, K. W. Chou, A. Drews, T. Tyliszczak, H. Stoll, B. Van Waeyenberge, and G. Meier, Phys. Rev. B **83**, 224422 (2011).

[26] A. Drews, B. Kruger, M. Bolte, and G. Meier, Phys. Rev. B **77**, 094413 (2008).

[27] A. Lyberatos, S. Komineas, and N. Papanicolaou, J. of Appl. Phys. **109**, 023911 (2011).

[28] T. Kamionka *et al.*, Phys. Rev. Lett. **105**, 137204 (2010).

[29] M. Pues, M. Martens, and G. Meier, J. of Appl. Phys. **116**, 153903 (2014).

[30] S. O. Demokritov and V. E. Demidov, IEEE Transactions on Magnetics **44**, 6 (2008).

[31] M. Asmat-Uceda, L. Li, A. Haldar, B. Shaw, and K. S. Buchanan, J. of Appl. Phys. **117**, 173902 (2015).

[32] V. E. Demidov, S. O. Demokritov, B. Hillebrands, M. Laufenberg, and P. P. Freitas, Appl. Phys. Lett. **85**, 2866 (2004).

[33] A. Vansteenkiste, J. Leliaert, M. Dvornik, M. Helsen, F. Garcia-Sanchez, and B. Van Waeyenberge, AIP Advances **4**, 107133 (2014).

[34] See Supplemental Material at [URL will be inserted by publisher], which includes annimations of selected dynamic modes of a magnetic antivortex.

[35] M. P. Kostylev, G. Gubbiotti, J. G. Hu, G. Carlotti, T. Ono, and R. L. Stamps, Phys. Rev. B **76**, 054422 (2007).

[36] C. E. Zaspel, B. A. Ivanov, J. P. Park, and P. A. Crowell, Phys. Rev. B **72**, 024427 (2005).

[37] K. Y. Guslienko and A. N. Slavin, J. Magn. Magn. Mater. **323**, 2418 (2011).

[38] The wavelength of the propagating wave was determined from plots of the amplitude and phase (e.g., see Supplementary Materials [34]). Note that these modes are within the detection range of the micro-BLS due to the larger wavelength across the wire.

[39] V. E. Demidov, J. Jersch, S. O. Demokritov, K. Rott, P. Krzysteczko, and G. Reiss, Phys. Rev. B **79**, 054417 (2009).